

Mesoporous TiO₂/Carbon Beads: One-Pot Preparation and Their Application in Visible-Light-Induced Photodegradation

Xiaowei Li · Yanqiu Jiang · Wenjing Cheng · Yudong Li · Xianzhu Xu · Kaifeng Lin

Received: 22 September 2014 / Accepted: 4 January 2015 / Published online: 24 March 2015
© The Author(s) 2015. This article is published with open access at Springerlink.com

Abstract Mesoporous TiO₂/Carbon beads have been prepared via a facile impregnation-carbonization approach, in which a porous anion-exchange resin and K₂TiO(C₂O₄)₂ were used as hard carbon and titanium source, respectively. Characterization results reveal that the self-assembled composites have disordered mesostructure, uniform mesopores, large pore volumes, and high surface areas. The mesopore walls are composed of amorphous carbon, well-dispersed and confined anatase or rutile nanoparticles. Some anatase phase of TiO₂ was transformed to rutile phase via an increase of carbonization temperature or repeated impregnation of the resin with TiO(C₂O₄)₂²⁻ species. X-ray photoelectron spectroscopy, carbon, hydrogen, and nitrogen element analysis, and thermal gravity analysis results indicate the doping of carbon into the TiO₂ lattice and strong interaction between carbon and TiO₂ nanoparticles. A synergy effect by carbon and TiO₂ in the composites has been discussed herein on the degradation of methyl orange under visible light. The dye removal process involves adsorption of the dye from water by the mesopores in the composites, followed by photodegradation on the separated dye-loaded catalysts. Mesopores allow full access of the dye molecules to the surface of TiO₂ nanoparticles. Importantly, the bead format of such composite enables their straightforward separation from the reaction mixture in their application as a liquid-phase heterogeneous photodegradation catalyst.

Keywords TiO₂ nanoparticles · Mesoporous carbon · Composite bead · Visible light · Easy separation

1 Introduction

Among various inorganic nanomaterials, titania (TiO₂) is regarded as the most promising photocatalysts in water splitting and the mineralization of toxic organic substances as its attractive features of low-cost, nontoxicity, and high stability [1–5]. For major applications, however, problems with the use of these TiO₂ nanoparticles are also well recognized: (1) titania absorbs only ultraviolet light; (2) the loss of the nanoparticles in solution and aggregation of the

nanoparticles in suspension. To improve the energy efficiency, several efforts have been made in developing new photocatalysts by modifying the TiO₂ sheets with nonmetal elements to narrow the band gap and enhance activities under visible light (>420 nm) [6–14]. Carbon modifications including carbon doping, carbon-related coating, and carbon loading have been touted as one of ideal and inexpensive choices for narrowing the band gap and increasing the visible light response of TiO₂ nanoparticles [15–18]. Despite the complexities in synthetic procedures, the carbon modified TiO₂ nanoparticles have shown higher photocatalytic activity than the non-modified analog during the degradation of substances under visible light. Among the modifications, TiO₂ nanoparticles loaded on carbons have been extensively investigated [19–22]. It has been proved that such composites have a large electron-storage capacity and can accept the photon-excited electrons to promote the separation of photo-generated carries. Besides,

X. Li · Y. Jiang · W. Cheng · Y. Li · X. Xu (✉) · K. Lin (✉)
Academy of Fundamental and Interdisciplinary Sciences, Harbin
Institute of Technology, Harbin 150080, People's Republic of
China
e-mail: xuxianzhu@hit.edu.cn

K. Lin
e-mail: linkaifeng@hit.edu.cn

TiO₂ in such materials could be sensitized by absorbing more visible light [23].

Soft and hard carbon sources have been used as the based materials and activated carbons to prepare the TiO₂/carbon (TiO₂/C) composites. For examples, Zhao et al. utilized furfural as the soft carbon source to synthesize carbon@TiO₂ with visible-light activity by solvothermal synthesis procedure [24]. In the photodegradation progress, the direct optical charge transfer transition was completed by both the carbon and TiO₂. Zhang et al. synthesized nano-sized TiO₂-supported activated carbon and realized the microwave-induced degradation of parathion with coal powder carbon precursor [25]. In order to overcome the drawback of the loss of TiO₂ nanoparticles in solution and aggregation of TiO₂ nanoparticles in suspension, active carbon sources with certain shape have been applied for preparation of such composites; however, most of them were investigated under ultraviolet (UV) light. Asiltürk et al. employed chemical activated pine sawdust as activated carbon support for TiO₂, and the materials exhibited high activities for the degradation of Rhodamine B under UV light [26]. Baek et al. used the spherical strong acid ion-exchange resin as carbon precursor to support TiO₂ and degrade humic acid under UV irradiation [27]. Shi et al. utilized rayon as the activated carbon fiber precursor and synthesized TiO₂/activated carbon fibers photocatalyst that degraded methylene blue under ultraviolet irradiation [28].

Inspired by the studies on the preparation of spherical carbon structures [29–31], herein, we report a one-pot approach for preparation of mesoporous TiO₂/C beads obtained by a facile anion-exchange progress and the subsequent carbonization procedure. Under visible light, the obtained beads exhibited high photocatalytic activity. More importantly, the separation of the beads from the reaction solution was extremely straightforward and did not require any centrifugation or filtration because the bead format was not destroyed during photocatalysis. This work may realize the wide application of TiO₂, and has a certain practical significance.

2 Experimental

2.1 Preparation of Photocatalysts

The incorporation of TiO₂ nanoparticles into the activated carbon matrix was performed by a general impregnation-carbonization approach, in which Amberlite IRA-900 resin and potassium titanium oxide oxalate dihydrate (K₂TiO(C₂O₄)₂·2H₂O) were used as carbon and titanium precursors, respectively. Amberlite IRA-900 resin is in the chloride form with bead size of 290–480 μm (measured by

optical microscope and determined by more than 50 beads), and is a strongly basic, macroreticular resin with moderately high porosity and with benzyltrialkylammonium functionalities [32]. The titanium precursor was purchased from Sinopharm Chemical Reagent Co., Ltd and was used without purification.

In a typical synthesis, 0.9 g of K₂TiO(C₂O₄)₂·2H₂O was mixed with 15 mL of deionized water, and stirred for 1 h at room temperature to obtain a clear solution. Next, 3 g of Amberlite IRA-900 resin beads were added to the solution. The mixture was stirred at room temperature for 12 h during the whole impregnation procedure. Then, the liquid was decanted and the beads were washed with deionized water and dried at 60 °C. The above-synthesized composite beads were transferred to a ceramic boat, placed in a tubular furnace, purged with nitrogen atmosphere and heated at 750, 900 °C for 4 h or 1,100 °C for 1 h at a rate of 2 °C min⁻¹. It was determined that control of the temperature was critical for effective carbonization of the composite beads. The resultant material was denoted as Meso-TiO₂/C-*x*-1, where *x* refers to the carbonization temperature. In other cases, Meso-TiO₂/C-*x*-2 were prepared by the same procedure for Meso-TiO₂/C-*x*-1, but using the resin derivatives before carbonization instead of starting IRA-900 resin beads in the impregnation process, that is, they were repeatedly impregnated in the solution of K₂TiO(C₂O₄)₂ with the same concentration (0.17 M). The resultant material was denoted as Meso-TiO₂/C-750-2, Meso-TiO₂/C-900-2 and Meso-TiO₂/C-1100-2, respectively. For comparison, IRA-carbon sample was prepared by direct carbonization of IRA-900 resin beads at 900 °C for 4 h.

2.2 Characterization

X-ray diffraction (XRD) patterns were measured on a Bruker D8 Advance powder diffractometer with using Cu Kα radiation (40 kV, 30 mA) for phase identification. The isotherms of nitrogen adsorption/desorption were measured at liquid nitrogen temperature using a Micromeritics TriStar 3000. The pore-size distribution was calculated using Barrett-Joyner-Halenda (BJH) model. Scanning electron microscopy (SEM) images were taken on a Hitachi S-4300 apparatus and secondary electron detector was used in the SEM measurement. Transmission electron microscopy (TEM) images were recorded on a Tecnai G² instrument operating at 300 kV. For the preparation of sample for TEM analysis, the beads were ground into powders and dispersed in ethanol, and then the suspension was sonicated for 10 min. One drop of the suspension was placed on a TEM grid, and allowed to dry overnight. X-ray photoelectron spectroscopy (XPS) measurements were recorded using a PHI 5000C ESCA system with Al Kα

radiation ($h\nu = 1,486.6$ eV). The electron take-off angle was 45° for all the samples, and the C1 *s* peak level was taken as internal reference at 284.6 eV. Elemental analyses of carbon content were performed on the elemental analyzer (Vario Micro Cube, Elementar). Thermal gravity analysis (TG) curves were monitored on a STA 449C apparatus. Ultraviolet–visible (UV/Vis) analysis was performed with a Perkin Elmer Lambda 750 spectrophotometer in matched cells.

2.3 Photocatalysis Test

The batch photoreactor was an open to air cylindrical flask and the visible light was provided by a 300 W Xe lamp with a UV cutoff filter ($\lambda > 420$ nm). Irradiation was filtered by a circulating water cell (thickness 5.0 cm) to remove IR beams thus preventing any heating of the suspension. 30 mg of the composite beads was dispersed into 50 mL of methyl orange (MO) solution (10 mg L^{-1}) under magnetic stirring at room temperature. Prior to the irradiation, the dispersion was kept in the dark for 30 min. Solutions were collected after every irradiation at certain time intervals and analyzed using a UV–vis spectrophotometer in matched quartz cells at 464 nm. For comparison, the reactions were carried out with the catalyst of P25 or IRA-carbon. The percentage of degradation was calculated as c/c_0 , where c is the concentration of the remaining dye solution at each irradiated time interval, while c_0 means the concentration of MO solution after keeping it in the dark for 30 min in the presence of any photocatalyst. Notably, the bead shape of Meso-TiO₂/C was unaffected during the photocatalytic tests. The beads were deposited automatically on the bottom of the vial a few seconds after stirring was stopped. Therefore, the beads could be easily separated from the reaction solution without centrifugation or filtration.

3 Results and Discussion

3.1 X-ray Diffraction Patterns

The crystalline structure of the TiO₂ phase was investigated using XRD. The XRD patterns of the Meso-TiO₂/C beads obtained at different carbonization temperatures are shown in Fig. 1. The IRA-carbon without TiO₂ impregnation is an amorphous phase at any given carbonization temperature (not shown here). At a carbonization temperature of 750 °C, the diffraction peaks are not well defined, indicating the low crystalline TiO₂ structural order in Meso-TiO₂/C-750-1. When the carbonization temperature is increased up to 900 °C, the peaks assigned to anatase (JCPDS No. 21-1272) become sharp, indicating the

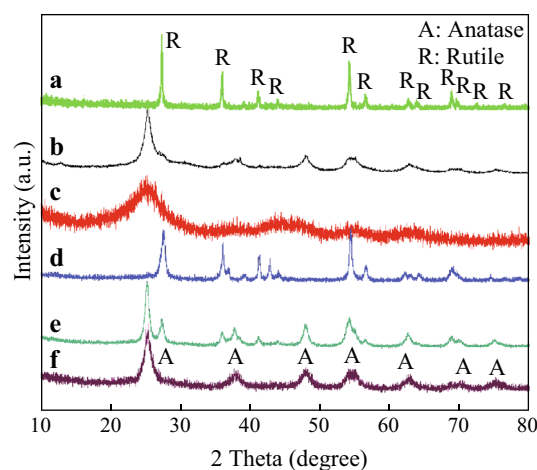


Fig. 1 XRD patterns of *a* Meso-TiO₂/C-1100-1, *b* Meso-TiO₂/C-900-1, *c* Meso-TiO₂/C-750-1, *d* Meso-TiO₂/C-1100-2, *e* Meso-TiO₂/C-900-2 and *f* Meso-TiO₂/C-750-2

formation of greater TiO₂ crystallites and enhancement of crystallization, and weak peaks at $2\theta = 27.58, 36.18, 41.38, 44.18,$ and 56.78 that correspond to rutile (JCPDS No. 21-1276) begin to appear in the case [33]. This observation suggests that certain amount of the anatase type may transform into the rutile type during the carbonization at 900 °C. When the carbonization temperature reaches 1,100 °C, as expected, complete transformation of anatase type to rutile is achieved. Clearly, it is found that carbonization temperature has a big influence on phase transformation of TiO₂, which is in agreement with the results reported before [33]. The average particle size of these TiO₂ crystallites can be estimated from the full widths at half-maximum of the (101) peak of anatase and the (110) peak of rutile by applying the Scherrer equation (Table 1), and it follows that the anatase crystallite size increases with increasing heat-treatment temperature, suggesting that high temperature leads to TiO₂ crystal growth.

For the bead samples of Meso-TiO₂/C-*x*-2 prepared by repeated impregnation process, some differences are noted between diffraction patterns of Meso-TiO₂/C-*x*-1 and Meso-TiO₂/C-*x*-2. Meso-TiO₂/C-750-2 possesses higher structural order than Meso-TiO₂/C-750-1; the rutile content of Meso-TiO₂/C-900-2 is larger than that of Meso-TiO₂/C-900-1; weak peaks at $2\theta = 36.7$ and 42.9 assigned to TiN crystals (JCPDS No. 38-1420) are shown in Meso-TiO₂/C-1100-2 [34]. These results suggest that repeated impregnation possibly result in enhanced exchange of negatively charged $\text{TiO}(\text{C}_2\text{O}_4)_2^{2-}$ species with anions in IRA-900.

3.2 SEM and TEM Images

The morphology and structure of Meso-TiO₂/C samples are clearly revealed by SEM and TEM images. After synthesis

Table 1 Characteristics of Meso-TiO₂/C photocatalysts prepared at different conditions

	Average particle size (nm) ^a	Mesopore size (nm) ^b	Mesopore volume (cm ³ g ⁻¹) ^b	Micropore volume (cm ³ g ⁻¹) ^c	Surface area (m ² g ⁻¹)	Carbon content (%) ^d
Meso-TiO ₂ /C-1100-1	40.4	3.9	0.36	0.04	433	41.7
Meso-TiO ₂ /C-1100-2	20.7	3.9	0.35	0.04	436	43.2
Meso-TiO ₂ /C-900-1	6.0	3.8	0.28	0.07	444	50.8
Meso-TiO ₂ /C-900-2	10.9	3.4; 19.0	0.38	0.05	541	40.7
Meso-TiO ₂ /C-750-1	–	–	–	–	20	57.7
Meso-TiO ₂ /C-750-2	6.9	–	–	–	4	46.4
IRA-carbon	–	–	0.03	0.33	741	94.6

^a Calculated by Scherrer equation

^b Calculated by BJH model

^c Calculated by t-plot analysis

^d Measured by CHN element analysis

and carbonization, Meso-TiO₂/C samples consist of hard and black beads. It has been observed that all samples contain a large amount of mesopores as well as a small quantity of macropores (Fig. 2), which might be created by the expansion of gases such as H₂O and CO_x that are formed during the carbonization at high temperatures (900–1,100 °C) under nitrogen. Although spherical carbon materials are also obtained when only IRA-900 resin beads are carbonized at 900 °C under nitrogen atmosphere, the size of IRA-carbon (80–210 μm) greatly decreases compared with that of IRA-900 (290–480 μm). This clearly reveals the supporting role of TiO₂ nanoparticles in the carbon matrix. In order to evaluate the size of these beads, the samples were characterized by optical images (Fig. 3). Based on the fact that more than fifty beads were calculated for each sample, the conclusion on the bead size of each sample was drawn in a statistical manner. Note that the size of Meso-TiO₂/C-1100-1 (110–240 μm) and Meso-TiO₂/C-1100-2 (115–250 μm) is smaller than that of other Meso-TiO₂/C beads (130–240 μm for Meso-TiO₂/C-900-1 and 130–260 μm for Meso-TiO₂/C-900-2), which suggests that shrinkage of resin-Ti composite beads is more pronounced during the carbonization at very high temperature (1,100 °C).

TEM images for Meso-TiO₂/C beads show typical images for a composite, in which a large amount of TiO₂ nanoparticles are well arranged in an amorphous carbon substance (Fig. 4). Based on the size distribution histogram, the size of nanoparticles in the composites follows the trend: Meso-TiO₂/C-1100-1 > Meso-TiO₂/C-1100-2 > Meso-TiO₂/C-900-2 > Meso-TiO₂/C-900-1, which is in agreement with the results obtained from XRD patterns. It seems that high carbonization temperature is favorable for larger particle size. Note here that TiO₂ particle size in Meso-TiO₂/C-1100-1 is much larger than that of Meso-TiO₂/C-1100-2 even though they were carbonized at the

same condition. As seen from the optical images, the bead shrinkage in Meso-TiO₂/C-1100-1 is more pronounced than in Meso-TiO₂/C-1100-2. In the case, preformed nanoparticles were possibly squeezed by the shrinkage of carbon matrix and then aggregated to form larger TiO₂ particles.

It has been also observed that disordered mesopores are clearly contained in the amorphous carbon substance, making channels for mass transport from the substance to the nanoparticles and/or large enough space for adsorption of substrates. Compared with similar results reported in mesoporous solids based titania, in which nanocrystals are randomly “glued” together by amorphous but not always mesoporous substances such as carbon, P₂O₅ and silica [35, 36], creation of mesopores in the carbon matrix corresponds to the utilization of the anion-exchange resin. From high-resolution transmission electron microscopy (HRTEM) images given in Fig. 4, the lattice fringe of the nanoparticles is 0.24 nm for Meso-TiO₂/C-1100-1 and Meso-TiO₂/C-1100-2, related to the (101) facet of rutile, and the value for Meso-TiO₂/C-900-1 and Meso-TiO₂/C-900-2 is about 0.36 nm, related to the (101) facet of anatase [20, 33]. It should be noted that the (004) facet of anatase with a d-spacing of 0.24 nm could also be observed in Meso-TiO₂/C-900-1, which are rarely reported in other anatase nanoparticles [21].

3.3 N₂ Adsorption/Desorption Isotherms

Figure 5 shows nitrogen adsorption/desorption isotherms for different Meso-TiO₂/C beads. Meso-TiO₂/C-900-1, Meso-TiO₂/C-1100-1, and Meso-TiO₂/C-1100-2 exhibit type IV isotherms with hysteresis loops at P/P₀ > 0.4. This reveals the presence of mesopores, consistent with TEM results. The mesopores in the samples may result from the expansion of gases such as H₂O and CO_x during the

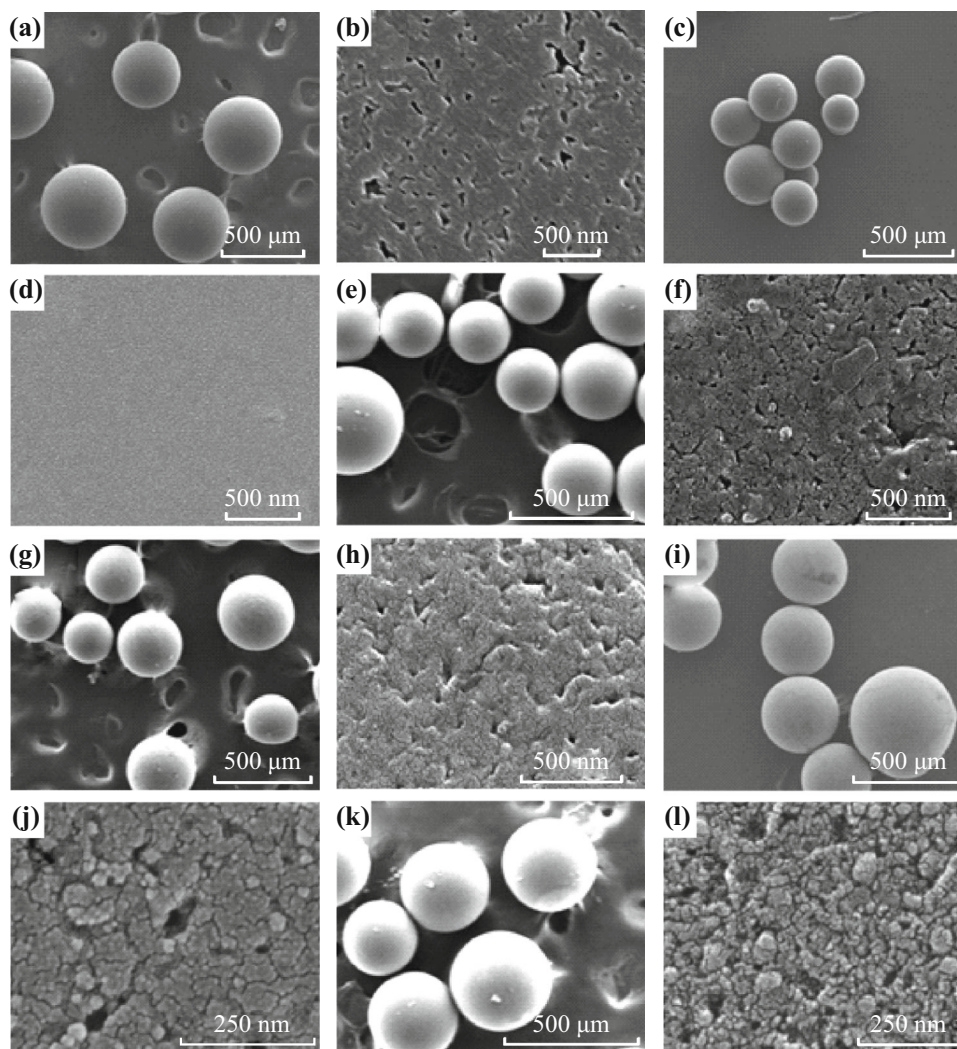


Fig. 2 SEM images of **a, b** IRA-900, **c, d** IRA-carbon, **e, f** Meso-TiO₂/C-1100-1, **g, h** Meso-TiO₂/C-1100-2, **i, j** Meso-TiO₂/C-900-1 and **k, l** Meso-TiO₂/C-900-2

carbonization [37]. In contrast, the N₂ adsorption/desorption isotherm of Meso-TiO₂/C-900-2 has an additional hysteresis loop above $P/P_0 = 0.8$, showing the presence of larger mesopores with a size at 18.9 nm. Combining with the TEM image of Meso-TiO₂/C-900-2 (Fig. 4g, h), these mesopores may correspond to the void space between TiO₂ nanoparticles and mesoporous carbon substance. Absence of such mesopores in other Meso-TiO₂/C beads might be due to the occurrence of more pronounced shrinkage of resin-Ti composite beads during the carbonization, which took place in the cases with higher temperature (1,100 °C) and/or lower TiO₂ content. As observed from Table 1 presenting texture properties, most of the bead samples in this work display high Brunauer–Emmet–Teller (BET) surface area and pore volume, which can favor mass transportation in the interior of the beads. It is worth noting that micropore volumes have been also estimated by

performing *t*-plot analysis. Compared with their mesopore volume, the carbons are mainly mesoporous though the micropores are present in each sample. Meso-TiO₂/C-750-1 and Meso-TiO₂/C-750-2 give very low BET surface areas (20 and 4 m² g⁻¹) and no mesopores are contained in them due to the relatively low carbonization temperature.

3.4 XPS and TG Results

The Meso-TiO₂/C beads obtained via carbonization at 900 and 1,100 °C showed Ti 2P_{3/2} and Ti 2P_{1/2} XPS peaks comparable to those of bulk and neat mesoporous TiO₂ though the signals are rather weaker in the spectra of Meso-TiO₂/C (Fig. 6), possibly due to immobilization of TiO₂ nanoparticles in mesopores of carbon. Notably, the spin-orbital splitting is 5.6 eV, which is slightly lower than that

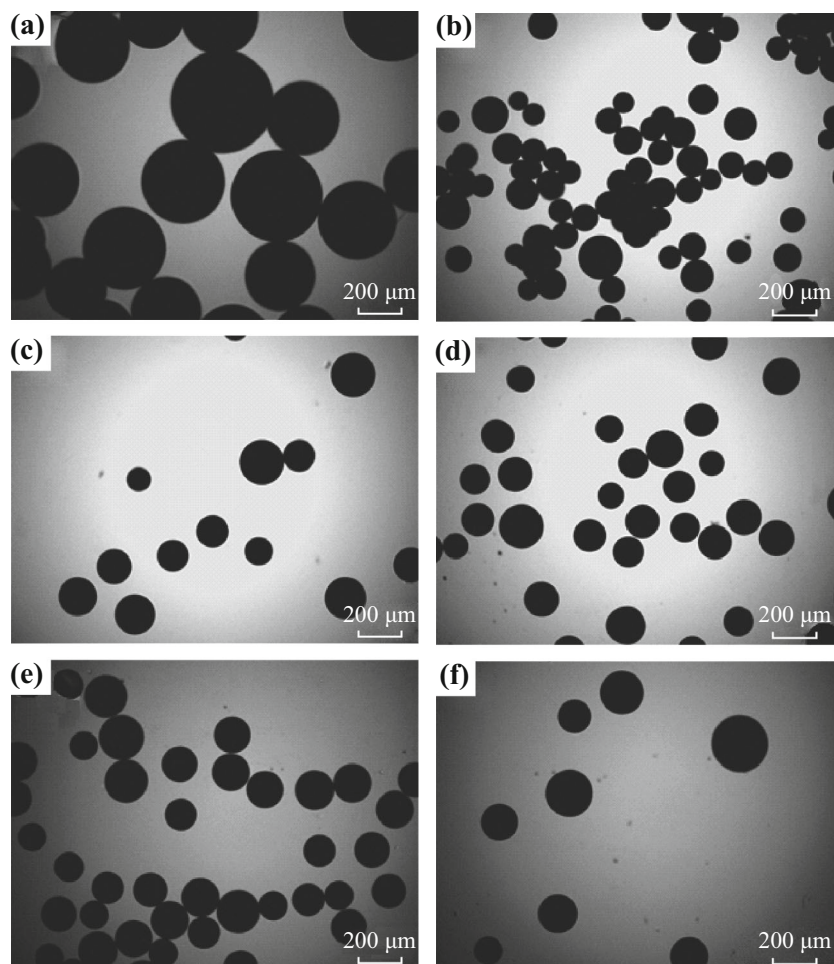


Fig. 3 Optical images of **a** IRA-900, **b** IRA-carbon, **c** Meso-TiO₂/C-1100-1, **d** Meso-TiO₂/C-1100-2, **e** Meso-TiO₂/C-900-1 and **f** Meso-TiO₂/C-900-2

in bulk anatase and mesoporous titania (5.8 eV). Similar observations have been reported for nonmetal-doped anatase, and were attributed to the introduction of differently hybridized atoms into the anatase crystal lattice [20, 21, 33]. Because no signals attributed to TiC (454.9 and 460.7 eV) were detected, carbon doping in the TiO₂ lattice is therefore responsible for the change in the spin-orbital splitting of TiO₂. These interstitial carbon atoms have been proved to improve the degree of separation and to restrain the recombination of photo-induced electron and hole carriers in carbon-doped TiO₂, which is conducive to improving the photocatalytic activity of the catalysts under visible-light illumination. Additionally, the interaction between carbon and TiO₂ nanoparticles may occur during the heat treatment.

Figure 7 shows the TG curves of Meso-TiO₂/C beads carried in air, which could not reach a platform value even at 800 °C, suggesting that carbonaceous materials were not burn off at high temperature. Compared with the observation that carbonaceous materials in Meso-TiO₂/C-750-1

were burn off at around 400–600 °C, the TG results of Meso-TiO₂/C beads prove the strong interaction between carbon and TiO₂ nanoparticles.

Depending on the characterization results, we suggest a possible path for the formation of Meso-TiO₂/C beads by the mean of anion-exchange resin beads (Scheme 1). The fabrication procedure for the bead format starts with treatment of the resin with aqueous solutions of the negatively charged TiO(C₂O₄)₂²⁻ species, in which the anionic species are bound onto the host resin through electrostatic interactions. The intercondensation of TiO(C₂O₄)₂²⁻ would determine the crystalline TiO₂ nanoparticles in large mesopores and macropores of the resin during the heat treatment, which leads to the formation of composite beads of TiO₂ nanoparticles and amorphous carbon. Simultaneously, the mesopores are generated from the gasification of volatile matter during the carbonization. Generally, the presence of mesopores in the amorphous carbon can significantly enhance adsorption capacities, especially for large adsorbates.

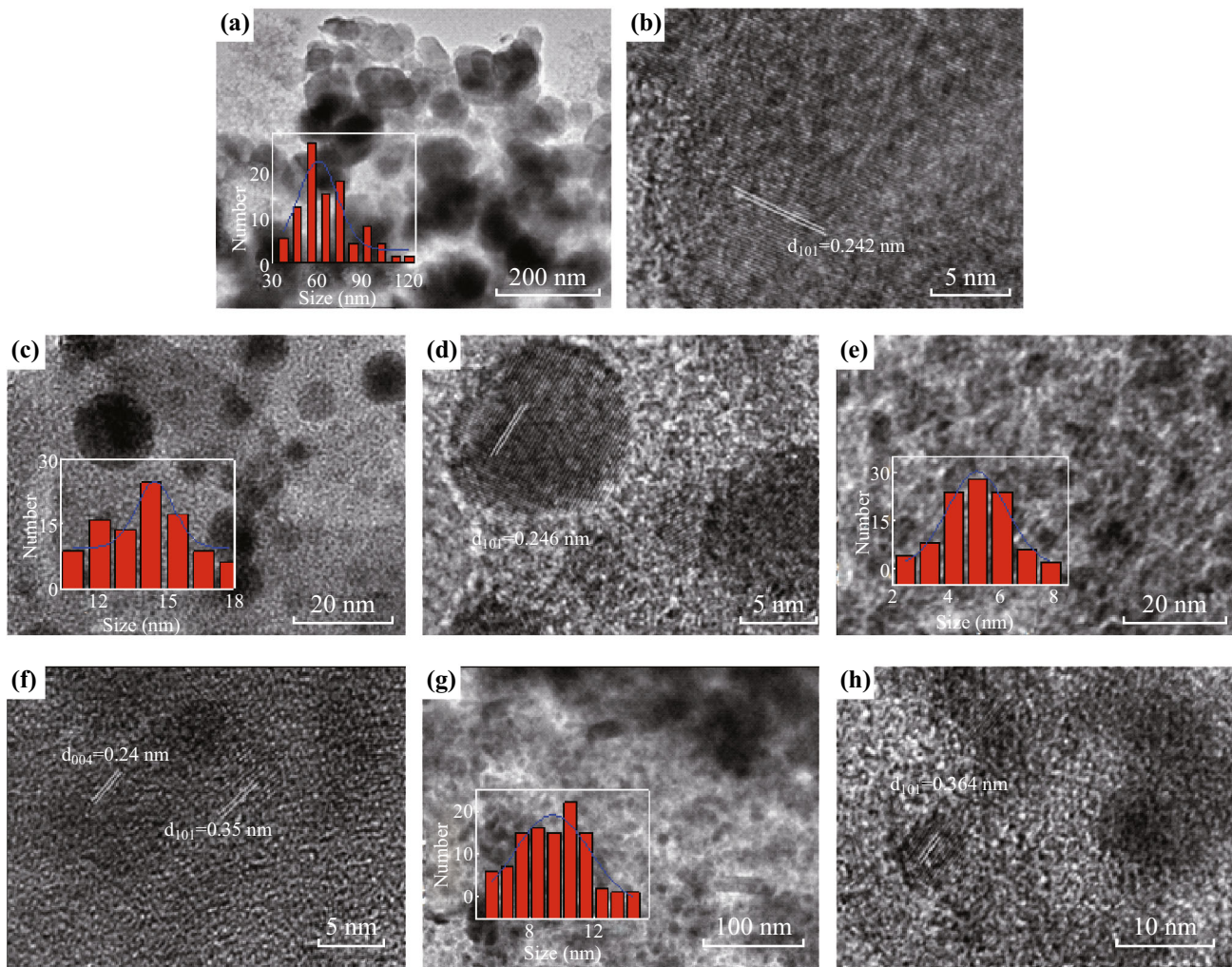


Fig. 4 TEM images of **a, b** Meso-TiO₂/C-1100-1, **c, d** Meso-TiO₂/C-1100-2, **e, f** Meso-TiO₂/C-900-1 and **g, h** Meso-TiO₂/C-900-2. Insets are size distribution (histogram) of TiO₂ nanoparticles in these composite beads

3.5 Photocatalytic Activity

The visible-light photocatalytic activity of Meso-TiO₂/C beads prepared at different carbonization temperature and impregnation process was evaluated, in which methyl orange was chosen as a degradation substrate for the adsorption and photocatalysis experiments. Before carrying out photodegradation tests, the adsorption capacity of the composite beads was tested. First, Meso-TiO₂/C-1,100-1 (50 mg) was kept in MO solution (50 mL; 10 mg L⁻¹) for 24 h and they were then separated from the solution without further washing, yielding dye-loaded Meso-TiO₂/C-1100-1. After being cooled in air overnight, the dye-loaded Meso-TiO₂/C-1100-1 was subjected to re-adsorption under the same concentration of MO solution. Such adsorption test was performed three times in total and each time MO molecules were almost adsorbed on Meso-TiO₂/C-1100-1 after 24 h. This clearly indicates that such bead

materials possess high adsorption capacity for MO due to their high surface areas and high pore volumes, and the saturated adsorption amount could hardly be reached under the conditions. This phenomenon also provides evidence of the high affinity between the adsorbate and the adsorbent.

To understand the nature of the catalytic center, we performed series of adsorption and catalysis tests for the degradation of the azo dye, which consisted of 100 min for adsorption in the dark and for illumination under visible light (Fig. 8). A blank experiment was carried out with the MO solution, without any photocatalytic material, proving that there is no direct photolysis of the dye molecules. Compared with their adsorption capacity, as observed from Fig. 8, the Meso-TiO₂/C samples carbonized at 900 and 1,100 °C have high visible-light photocatalytic activity. Prior to the irradiation, the dispersion was kept in the dark for 30 min. About 21, 36, 27, and 23 % of the dye calculated by c/c_0 was adsorbed on Meso-TiO₂/C-900-1, Meso-

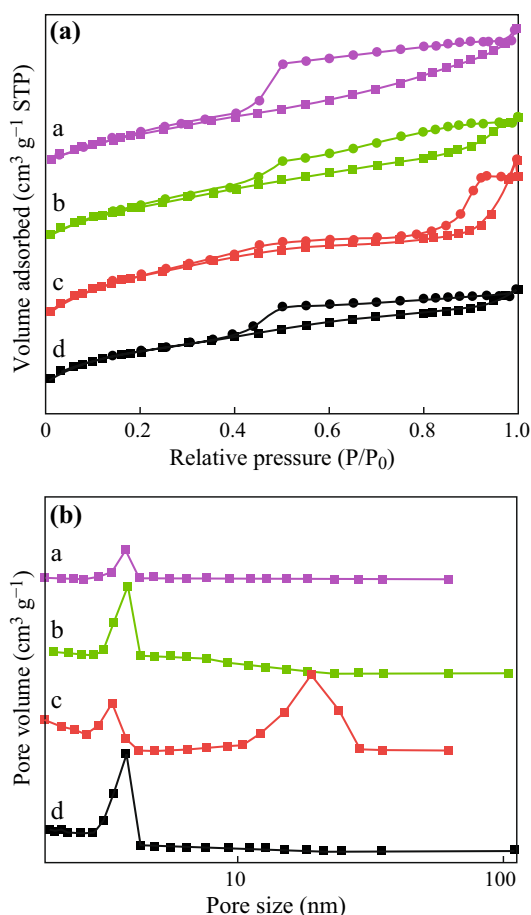


Fig. 5 **a** Nitrogen adsorption (filled square)/desorption (filled circle) isotherms and **b** Pore-size distribution curves calculated from desorption branch of Meso-TiO₂/C-1100-2 (*a*), Meso-TiO₂/C-1100-1 (*b*), Meso-TiO₂/C-900-2 (*c*) and Meso-TiO₂/C-900-1 (*d*)

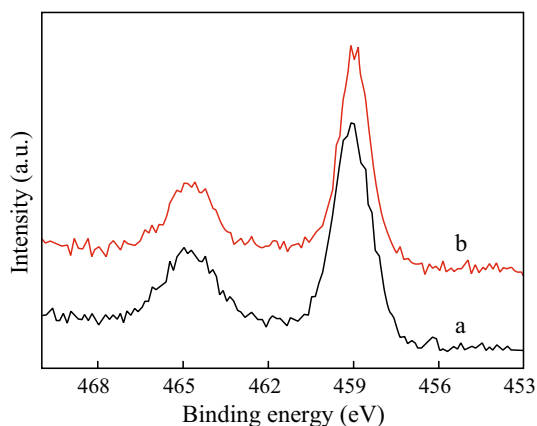


Fig. 6 Ti 2p XPS spectra of *a* Meso-TiO₂/C-900-2 and *b* Meso-TiO₂/C-1100-1

TiO₂/C-900-2, Meso-TiO₂/C-1100-1, and Meso-TiO₂/C-1100-2, respectively. With the extension of the illumination time, the degradation efficiency dramatically

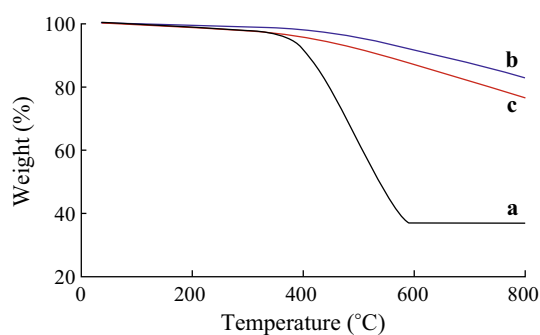
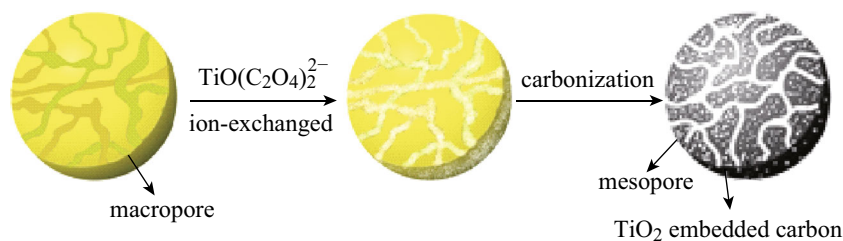


Fig. 7 TG curves of *a* Meso-TiO₂/C-750-1, *b* Meso-TiO₂/C-900-1 and *c* Meso-TiO₂/C-900-2

increased, reflecting degradation of the residue dye in the mesopores of Meso-TiO₂/C. After 100 min of illumination time, about 50–90 % of the dye was eliminated due to the simultaneous adsorption and photocatalysis. These observations illustrate that the dyes adsorbed in mesoporous carbon-titania composite beads can be degraded by crystalline TiO₂ nanoparticles inside carbon pore walls under visible light. Once the dyes in pores are mineralized, the occupied pores are empty, thus, enough space can be provided again for re-adsorption. These features may be attributed to the synergetic effects of the factors in terms of mesopores, the doping of carbon element into TiO₂ lattice and interaction between the carbon and TiO₂ [20, 34]. The mesopores in the interior favor the absorption of MO and simultaneously cause the MO molecules close to the TiO₂ nanoparticles. The carbon doping increases the visible-light absorption. This implies that Meso-TiO₂/C beads can be activated by visible light and more photo-generated electrons and holes can be created and participate in the photocatalytic reactions. Some other parallel experiments were also carried out on P25 and IRA-carbon (Fig. 9). Combined with the result that Meso-TiO₂/C-750-1 and Meso-TiO₂/C-750-2 exhibited low adsorption capacity and photocatalytic activity, proving that the mesopores in the beads play an important role in high adsorption capacity and that the doping of C element and/or interaction between mesoporous carbon and crystalline titania nanoparticles is vital for visible-light-induced degradation of the azo dye methyl orange. The photocatalytic activity (at reaction time of 100 min) of these composites follows the trend: Meso-TiO₂/C-900-2 > Meso-TiO₂/C-1100-1 > Meso-TiO₂/C-900-1 > Meso-TiO₂/C-1100-2 >> Meso-TiO₂/C-750-2 and Meso-TiO₂/C-750-1 (Fig. 8), indicating that the TiO₂ content, mesopore volume and the interaction between TiO₂ nanoparticles and carbon have significant influence on the photocatalytic activity and that anatase and rutile are both active for dye degradation under visible light.

Some researchers reported that photocatalytic reaction occurred under irradiation with visible light with active



Scheme 1 Possible schematic of the synthetic procedure for Meso-TiO₂/C

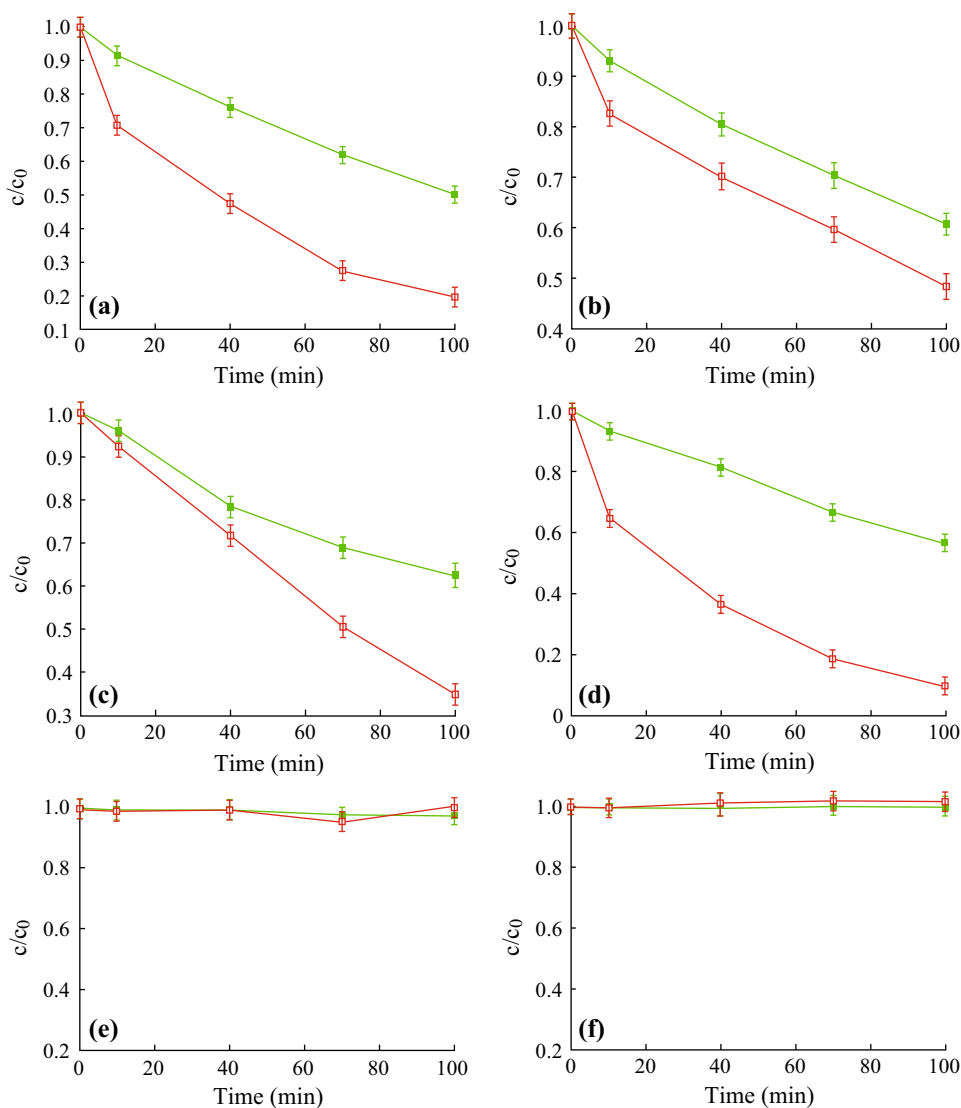


Fig. 8 Adsorption (filled square) and degradation (open square) rate for methyl orange on the catalysts **a** Meso-TiO₂/C-1100-1, **b** Meso-TiO₂/C-1100-2, **c** Meso-TiO₂/C-900-1, **d** Meso-TiO₂/C-900-2, **e** Meso-TiO₂/C-750-1 and **f** Meso-TiO₂/C-750-2 as a function of the contacting time

carbon samples and systems of condensed benzene rings in active carbon play the role of the organic semiconductor molecules [38]. However, in our case, IRA-carbon did not exhibit photocatalytic activity of MO under visible light. It is clear that the visible-light activity of the Meso-TiO₂/C beads should be described by taking into account other parameters. An explanation lies on the carbon doping into

the TiO₂ lattice during the formation of the composite beads, which is expected to favor lowering the bandgap energy of Meso-TiO₂/C composites. Consequently, significant enhancement in the photoactivity under visible light was obtained, as the researches described elsewhere [20, 33]. The carbonaceous species formed by doped C atoms acted as a photosensitizer, which can be excited and

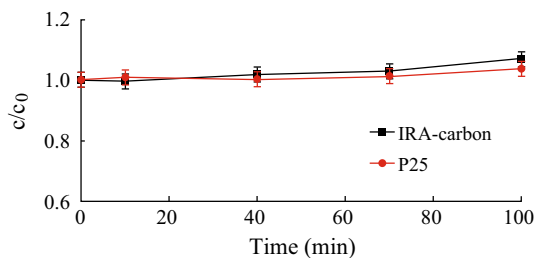


Fig. 9 Degradation rate for methyl orange on P25 and IRA-carbon as a function of the contacting time

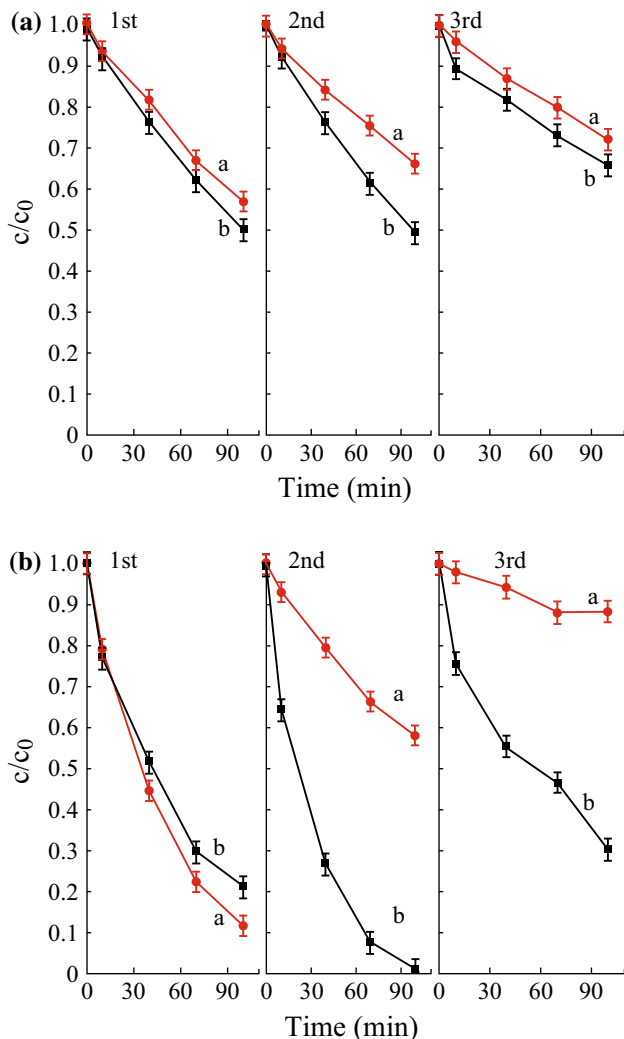


Fig. 10 Recycling runs in **a** adsorption and **b** photodegradation of methyl orange over Meso-TiO₂/C-900-2 and Meso-TiO₂/C-1100-1

inject electrons into the conduction band of TiO₂, then the electron is transferred to the molecular oxygen adsorbed in the mesopores of Meso-TiO₂/C, producing $\cdot\text{O}_2^-$ and $\cdot\text{OH}$ radicals that are capable of degrading MO [39]. An additional reason for the high visible-light activity of the Meso-TiO₂/C beads may be attributed to the strong interaction

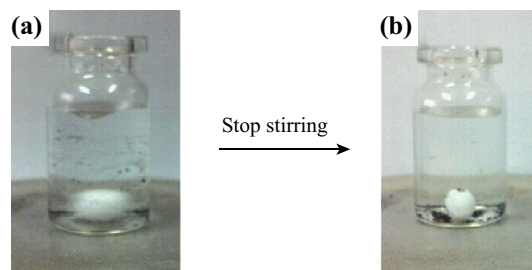


Fig. 11 Meso-TiO₂/C-1100-1 **a** under stirring and **b** in static conditions (a few seconds after stopping the stirring)

between carbon and TiO₂ nanoparticles [20, 21, 33]. It is well known that amorphous carbonaceous material is a kind of strongly dye-absorbing carbons. In the present work, methyl orange adsorbed in the mesopores of the Meso-TiO₂/C beads can absorb visible light and is excited, which is similar as the results reported elsewhere [20, 21, 33]. In addition, the enriched and excited dye molecules in the mesopores can fully access active crystalline titania nanoparticles via the present mesopore channels. It has been proved that the conduction band of TiO₂ plays an important role and the appropriate corresponding potential enables the excited dye molecules to inject electrons into the conduction band of a TiO₂ particle [39]. It is supposed, thus, carbon doping modifies the bandgap of crystalline TiO₂ nanoparticles, and may facilitate the above electron-injection process, yielding dye radicals. These dye radicals are transient, active species and decompose into small molecules and ever further to CO₂ by complicated reactions involving oxygen.

In view of potential industrial applications, recyclability is an important parameter in evaluating a catalyst. It has been well known that TiO₂ nanoparticles are hard to separate from the aqueous or gaseous pollutants and aggregate easily in suspension, which would significantly affect the activity and stability of the photocatalyst. To complete the evaluation of our novel catalyst Meso-TiO₂/C beads, the materials were recovered from the reaction mixture and reused in several photocatalytic cycles (Fig. 10). The straightforward recycling procedure for Meso-TiO₂/C beads only required washings in ethanol at room temperature without any calcination. Note that the bead shape of Meso-TiO₂/C was unaffected by stirring during the catalytic tests. The beads were deposited automatically on the bottom of the vial a few seconds after stirring stopped (Fig. 11). Therefore, the beads could be easily separated from the reaction solution without centrifugation or filtration. The catalytic activity of Meso-TiO₂/C-1100-1 remained at 85 % of the first run after three cycles, indicative of the good stability of the Meso-TiO₂/C beads catalyst. Interestingly, in the second run, reused Meso-TiO₂/C-1100-1 surprisingly displayed higher photocatalytic activity than

the fresh one, which is possibly because more facets of TiO₂ particles are exposed during stirring in the photocatalysis test. The reused Meso-TiO₂/C-1100-1 was characterized by TEM and no big difference on TiO₂ particles was observed compared with those in the fresh sample. Therefore, further investigation for its reusability is still in progress.

4 Conclusion

Mesoporous TiO₂/C composite beads have been prepared using anion-exchange resin as carbon source and applied as an adsorbent–photocatalyst to eliminate methyl orange under visible light. Dispersed TiO₂ nanoparticles were confined by mesoporous carbon pore walls, which prevented their aggregation during heating, and served to modify their surface and electronic structure. The composites showed a synergy effect by carbon and TiO₂ nanoparticles on elimination of the dye from water, that is, large mesopore size and high surface area facilitate the adsorption of the dye and well-dispersed TiO₂ nanoparticles are active to degrade dye molecules through the interface between carbon and TiO₂ nanoparticles. Also, mesopores allowed full access of the dye molecules to the surface of TiO₂ nanoparticles, where they were degraded. As a result of these unique features, the composite showed both high adsorption capacity and visible-light-induced photocatalytic activity. The doping of carbon into the TiO₂ lattice and strong interaction between carbon and TiO₂ nanoparticles has been proved to improve the photodegradation performances toward dyes. Notably, these mesoporous TiO₂/C composites could be easily separated from the dye solution due to their bead format, which is more attractive for industrial treatment of organic contaminants.

Acknowledgments This work was supported by Natural Science Foundation of China (21303031, 21353004, 51472062), Natural Science Foundation of Heilongjiang Province of China (B201010), Fundamental Research Funds for the Central Universities (HIT-IBRSEM. 201326), Program for Science & Technology Innovation Talent in Harbin (2013RFQXJ004, 2007RFXXG018) and China Postdoctoral Science Foundation (2012T50334, 20100480991).

Open Access This article is distributed under the terms of the Creative Commons Attribution License which permits any use, distribution, and reproduction in any medium, provided the original author(s) and the source are credited.

References

1. W. Zhao, Y. Sun, F.N. Castellano, Visible-light induced water detoxification catalyzed by Pt II dye sensitized titania. *J. Am. Chem. Soc.* **130**(38), 12566–12567 (2008). doi:10.1021/ja803522v
2. X. Wang, K. Maeda, A. Thomas, K. Takanebe, G. Xin, J.M. Carlsson, K. Domen, M. Antonietti, A metal-free polymeric photocatalyst for hydrogen production from water under visible light. *Nat. Mater.* **8**(1), 76–80 (2009). doi:10.1038/nmat2317
3. W. Zhao, W. Ma, C. Chen, J. Zhao, Z. Shuai, Efficient degradation of toxic organic pollutants with Ni₂O₃/TiO₂-xBx under visible irradiation. *J. Am. Chem. Soc.* **126**(15), 4782–4783 (2004). doi:10.1021/ja0396753
4. G. Liu, L. Wang, H. Yang, H. Cheng, G. Lu, Titania-based photocatalysts-crystal growth, doping and hetero structuring. *J. Mater. Chem.* **20**(5), 831–843 (2010). doi:10.1039/b909930a
5. Q. Xiang, J. Yu, M. Jaroniec, Graphene-based semiconductor photocatalysts. *Chem. Soc. Rev.* **41**(2), 782–796 (2012). doi:10.1039/c1cs15172j
6. R. Asahi, T. Morikawa, T. Ohwaki, K. Aoki, Y. Taga, Visible-light photocatalysis in nitrogen-doped titanium oxides. *Science* **293**(5528), 269–271 (2001). doi:10.1126/science.1061051
7. F. Wei, L. Ni, P. Cui, Preparation and characterization of N-S-codoped TiO₂ photocatalyst and its photocatalytic activity. *J. Hazard. Mater.* **156**(1–3), 135–140 (2008). doi:10.1016/j.jhazmat.2007.12.018
8. Y. Cong, X. Li, Y. Qin, Z. Dong, G. Yuan, Z. Cui, X. Lai, Carbon-doped TiO₂ coating on multiwalled carbon nanotubes with higher visible light photocatalytic activity. *Appl. Catal. B-Environ.* **107**(1–2), 128–134 (2011). doi:10.1016/j.apcatb.2011.07.005
9. D. Chen, Z. Jiang, J. Geng, Q. Wang, D. Yang, Carbon and nitrogen Co-doped TiO₂ with enhanced visible-light photocatalytic activity. *Ind. Eng. Chem. Res.* **46**(9), 2741–2746 (2007). doi:10.1021/ie061491k
10. S.C. Pillai, P. Periyat, R. George, D.E. McCormack, M.K. Seery, H. Hayden, J. Colreavy, D. Corr, S.J. Hinder, Synthesis of high-temperature stable anatase TiO₂ photocatalyst. *J. Phys. Chem. C* **111**(4), 1605–1611 (2007). doi:10.1021/jp065933h
11. H. Zang, R. Zong, J. Zhao, Y. Zhu, Dramatic visible photocatalytic degradation performances due to synergetic effect of TiO₂ with PANI. *Environ. Sci. Technol.* **42**(10), 3803–3807 (2008). doi:10.1021/es703037x
12. L. Gu, J.Y. Wang, R. Qi, X.Y. Wang, P. Xu, X.J. Han, A novel incorporating style of polyaniline/TiO₂ composites as effective visible photocatalysts. *J. Mol. Catal. A-Chem.* **357**, 19–25 (2012). doi:10.1016/j.molcata.2012.01.012
13. D. Landy, I. Mallard, A. Ponchel, E. Monflier, S. Fourmentin, Remediation technologies using cyclodextrins: an overview. *Environ. Chem. Lett.* **10**(3), 225–237 (2012). doi:10.1007/s10311-011-0351-1
14. R. Bleta, A. Lannoy, C. Machut, E. Monflier, A. Ponchel, Understanding the role of cyclodextrins in the self-Assembly, crystallinity, and porosity of titania nanostructures. *Langmuir* **30**(39), 11812–11822 (2014). doi:10.1021/la502911v
15. J.H. Park, S. Kim, A.J. Bard, Novel carbon-doped TiO₂ nanotube arrays with high aspect ratios for efficient solar water splitting. *Nano Lett.* **6**(1), 24–28 (2006). doi:10.1021/nl051807y
16. S. Sakthivel, H. Kisch, Daylight photocatalysis by carbon-modified titanium dioxide. *Angew. Chem. Int. Ed.* **42**(40), 4908–4911 (2003). doi:10.1002/anie.200351577
17. F. Dong, H. Wang, Z. Wu, One-step “green” synthetic approach for mesoporous C-doped titanium dioxide with efficient visible light photocatalytic activity. *J. Phys. Chem. C* **113**(38), 16717–16723 (2009). doi:10.1021/jp9049654
18. S. Liu, J. Yu, M. Jaroniec, Tunable photocatalytic selectivity of hollow TiO₂ microspheres composed of anatase polyhedra with exposed 001 facets. *J. Am. Chem. Soc.* **132**, 11914–11916 (2010). doi:10.1021/jp9049654
19. C.H. Kim, B.H. Kim, K.S. Yang, TiO₂ nanoparticles loaded on graphene/carbon composite nanofibers by electrospinning for

- increased photocatalysis. *Carbon* **50**(7), 2472–2481 (2012). doi:[10.1016/j.carbon.2012.01.069](https://doi.org/10.1016/j.carbon.2012.01.069)
20. W. Wei, C. Yu, Q. Zhao, G. Li, Y. Wan, Improvement of the visible-light photocatalytic performance of TiO₂ by carbon mesostructures. *Chem. Eur. J.* **19**(2), 566–577 (2013). doi:[10.1002/chem.201202691](https://doi.org/10.1002/chem.201202691)
 21. W. Wei, C. Yu, Q. Zhao, X. Qian, G. Li, Y. Wan, Synergy effect in photodegradation of contaminants from water using ordered mesoporous carbon-based titania catalyst. *Appl. Catal. B-Environ.* **146**, 151–161 (2014). doi:[10.1016/j.apcatb.2013.04.048](https://doi.org/10.1016/j.apcatb.2013.04.048)
 22. J. Matos, A. Garcia, P.S. Poon, Environmental green chemistry applications of nanoporous carbons. *J. Mater. Sci.* **45**, 4934–4944 (2010). doi:[10.1007/s10853-009-4184-2](https://doi.org/10.1007/s10853-009-4184-2)
 23. G. Zhang, F. Teng, Y. Wang, P. Zhang, C. Gong, L. Chen, C. Zhao, E. Xie, Preparation of carbon-TiO₂ nanocomposites by a hydrothermal method and their enhanced photocatalytic activity. *RSC Adv.* **3**, 24644–24649 (2013). doi:[10.1039/c3ra44950e](https://doi.org/10.1039/c3ra44950e)
 24. L. Zhao, X. Chen, X. Wang, Y. Zhang, W. Wei, Y. Sun, M. Antonietti, M.M. Titirici, One-Step solvothermal synthesis of a carbon@TiO₂ dyade structure effectively promoting visible-light photocatalysis. *Adv. Mater.* **22**(30), 3317–3321 (2010). doi:[10.1002/adma.201000660](https://doi.org/10.1002/adma.201000660)
 25. Z. Zhang, J. Jiatieli, D. Liu, F. Yu, S. Xue, W. Gao, Y. Li, D.D. Dionysiou, Microwave induced degradation of parathion in the presence of supported anatase- and rutile-TiO₂/AC and comparison of their catalytic activity. *Chem. Eng. J.* **231**, 84–93 (2013). doi:[10.1016/j.cej.2013.07.001](https://doi.org/10.1016/j.cej.2013.07.001)
 26. M. Asilturk, S. Sener, TiO₂-activated carbon photocatalysts: Preparation, characterization and photocatalytic activities. *Chem. Eng. J.* **180**, 354–363 (2012). doi:[10.1016/j.cej.2011.11.045](https://doi.org/10.1016/j.cej.2011.11.045)
 27. M.H. Baek, W.C. Jung, J.W. Yoon, J.S. Hong, Y.S. Lee, J.K. Suh, Preparation, characterization and photocatalytic activity evaluation of micro- and mesoporous TiO₂/spherical activated carbon. *J. Ind. Eng. Chem.* **19**(2), 469–477 (2013). doi:[10.1016/j.jiec.2012.08.026](https://doi.org/10.1016/j.jiec.2012.08.026)
 28. J. Shi, H. Cui, J. Chen, M. Fu, B. Xu, H. Luo, Z. Ye, TiO₂/activated carbon fibers photocatalyst: Effects of coating procedures on the microstructure, adhesion property, and photocatalytic ability. *J. Colloid Interface Sci.* **388**(1), 201–208 (2012). doi:[10.1016/j.jcis.2012.08.038](https://doi.org/10.1016/j.jcis.2012.08.038)
 29. Z. Tan, Z.H. Sun, Q. Guo, H.H. Wang, D.S. Su, A novel ion-exchange method for the synthesis of nano-SnO/micro-C hybrid structure as high capacity anode material in lithium ion batteries. *J. Mater. Sci. Technol.* **29**(7), 609–612 (2013). doi:[10.1016/j.jmst.2013.04.001](https://doi.org/10.1016/j.jmst.2013.04.001)
 30. Z. Tan, Z.H. Sun, H.H. Wang, Q. Guo, D.S. Su, Fabrication of porous Sn-C composites with high initial coulomb efficiency and good cyclic performance for lithium ion batteries. *J. Mater. Chem. A* **1**(33), 9462–9468 (2013). doi:[10.1039/c3ta10524e](https://doi.org/10.1039/c3ta10524e)
 31. J. Zhang, R. Wang, E.Z. Liu, X.F. Gao, Z.H. Sun, F.S. Xiao, F. Girgsdies, D.S. Su, Spherical structures composed of multiwalled carbon nanotubes: formation mechanism and catalytic performance. *Angew. Chem. Int. Edit.* **51**(30), 7581–7585 (2012). doi:[10.1002/anie.201200969](https://doi.org/10.1002/anie.201200969)
 32. K. Lin, O.I. Lebedev, G.V. Tendeloo, P.A. Jacobs, P.P. Pescarmona, Titanosilicate beads with hierarchical porosity: synthesis and application as epoxidation catalysts. *Chem. Eur. J.* **16**(45), 13509–13518 (2010). doi:[10.1002/chem.201001508](https://doi.org/10.1002/chem.201001508)
 33. S.K. Parayil, H.S. Kibombo, C. Wu, R. Peng, J. Baltrusaitis, R.T. Koodali, Enhanced photocatalytic water splitting activity of carbon-modified TiO₂ composite materials synthesized by a green synthetic approach. *Int. J. Hydrogen Energy* **37**(10), 8257–8267 (2012). doi:[10.1016/j.ijhydene.2012.02.067](https://doi.org/10.1016/j.ijhydene.2012.02.067)
 34. G. Zhao, C. Zhao, L. Wu, G. Duan, J. Wang, G. Han, Study on the electrical and optical properties of vanadium doped TiN thin films prepared by atmospheric pressure chemical vapor. *J. Alloy. Compd.* **569**, 1–5 (2013). doi:[10.1016/j.jallcom.2013.03.110](https://doi.org/10.1016/j.jallcom.2013.03.110)
 35. R. Liu, Y. Ren, Y. Shi, F. Zhang, L. Zhang, B. Tu, D. Zhao, Controlled synthesis of ordered mesoporous C-TiO₂ nanocomposites with crystalline titania frameworks from organic-inorganic-amphiphilic coassembly. *Chem. Mater.* **20**(3), 1140–1146 (2008). doi:[10.1021/cm071470w](https://doi.org/10.1021/cm071470w)
 36. P. Chang, C. Huang, R.A. Doong, Ordered mesoporous carbon-TiO₂ materials for improved electrochemical performance of lithium ion battery. *Carbon* **50**(11), 4259–4268 (2012). doi:[10.1016/j.carbon.2012.05.009](https://doi.org/10.1016/j.carbon.2012.05.009)
 37. Z. Sun, L. Wang, P. Liu, S. Wang, B. Sun, D. Jiang, F. Xiao, Magnetically motive porous sphere composite and its excellent properties for the removal of pollutants in water by adsorption and desorption cycles. *Adv. Mater.* **18**(15), 1968–1971 (2006). doi:[10.1002/adma.200600337](https://doi.org/10.1002/adma.200600337)
 38. A.E. Eliyas, L. Ljutzkanov, I.D. Stambolova, V.N. Blaskov, S.V. Vassilev, E.N. Razkazova-Velkova, D.R. Mehandjiev, Visible light photocatalytic activity of TiO₂ deposited on activated carbon. *Cent. Eur. J. Chem.* **11**(3), 464–470 (2013). doi:[10.2478/s11532-012-0183-2](https://doi.org/10.2478/s11532-012-0183-2)
 39. G. Dai, S. Liu, Y. Liang, H. Liu, Z. Zhong, A simple preparation of carbon and nitrogen co-doped nanoscaled TiO₂ with exposed 001 facets for enhanced visible-light photocatalytic activity. *J. Mol. Catal. A* **368**, 38–42 (2013). doi:[10.1016/j.molcata.2012.11.014](https://doi.org/10.1016/j.molcata.2012.11.014)